Numerical Studies on Coupled Stokes-Transport Systems for Mantle Convection

Ponsuganth Ilangovan[0009−0008−8682−1307], Eugenio D'Ascoli, Nils Kohl[0000−0003−4797−0664], and Marcus Mohr[0000−0003−2942−8484]

Dept. of Earth and Environmental Sciences, LMU Munich, Germany p.ilango@lmu.de

Abstract. Accurate retrodictions of the past evolution of convection in the Earth's mantle are crucial to obtain a qualitative understanding of this central mechanism behind impactful geological events on our planet. They require highly resolved simulations and therefore extremely scalable numerical methods. This paper applies the massively parallel matrix-free finite element framework HyTeG to approximate solutions to stationary Stokes systems and time-dependent, coupled convection problems. It summarizes the underlying mathematical model and verifies the implementation through semi-analytical setups and community benchmarks. The numerical results agree with the expected outcomes from the literature.

Keywords: Mantle Convection · Finite Elements · Matrix-Free Methods

1 Introduction

Mantle convection is the dominant mechanism of heat transfer from Earth's hot outer core to the cold lithosphere. This movement is the major driving force for plate tectonics and, thus, finally the trigger of earthquakes and other geological events, such as mountain building and back-arc volcanism, [9]. Modelling this mechanism opens up pathways towards answering fundamental geophysical questions [5]. A model that accurately represents mantle convection can be used inversely, with the adjoint method, to determine the past state of our planet from present-day observations, especially seismic data. Such retrodictions can help us to narrow the range of physical parameters of the mantle and identifying the location of oil deposits, among other things, [15].

On geological time scales the mantle behaves like a highly viscous fluid. The governing equations, thus, involve the Stokes system, which is a simplification of the Navier-Stokes equations for nearly vanishing Reynolds numbers [16]. Buoyancy, resulting from thermo-chemical density differences in the mantle, is the primary driving force of convection. In addition to the motion of the mantle, one also needs to consider the evolution of heat, [7], which can be described by an advection-diffusion equation. Standard formulations can be found in literature for both compressible and incompressible models, [23, 25].

Accurate predictions require highly resolved simulations that can only be executed on massively parallel computers using extremely scalable numerical

ICCS Camera Ready Version 2024
To cite this paper please use the final published version:
DOI: 10.1007/978-3-031-63759-9_33

methods of optimal complexity. Resolving Earth's mantle globally with a resolution of 1 km requires meshes with trillions (10^{12}) of cells and yields linear systems of corresponding size. This is crucial to resolve small-scale features such as rising plumes and subducting slabs, but also to capture sharp viscosity changes between the lithosphere and underlying asthenosphere (4–5 orders of magnitude), and the resulting short wavelength asthenosphere dynamics [4].

We therefore employ the massively parallel matrix-free finite element software framework HyTeG [18, 21] to discretize the governing equations and solve the corresponding discrete problems. Its extreme-scalability has been demonstrated in, e.g., [19, 20].

The central focus of this paper is the evaluation and verification of the accuracy of the software through simulation of various benchmarks from mantle convection. We consider semi-analytic solutions to the stationary Stokes problem involving the relevant boundary conditions [22], two community benchmarks for time-dependent settings [3, 26], and eventually present results from a forward simulation of a compressible model. All development is driven by the TerraNeo project [1], which is an effort to create a scalable and accurate Earth model for the Geodynamics community.

2 Model and Formulation

On geologic time-scales the Earth's mantle behaves like a fluid. Its motion can, thus, be described by the Navier-Stokes equations. However, convection in the mantle is characterised by a very small Reynolds number $\mathcal{O}(10^{-15})$, i.e. the ratio of inertial to viscous forces, and an Ekmann number of $\mathcal{O}(10^{9})$, i.e. the ratio of viscous to Coriolis forces. Together this allows to neglect inertial and Coriolis forces and assume an instantaneous balance of viscous and buoyancy forces, resulting in a quasi-static flow field, [27]. Thus, one arrives at the momentum part of the Stokes equations

$$-\nabla \cdot \tau + \nabla p = \rho \mathbf{g} \tag{1}$$

with the deviatoric stress tensor τ, pressure p, density ρ and gravitational acceleration $\mathbf{g}$. Using the strain-rate tensor $\dot{\epsilon} = \frac{1}{2}\left(\nabla \mathbf{u} + (\nabla \mathbf{u})^{\top}\right)$ one can re-write the stress as

$$\tau = 2\eta\left(\dot{\epsilon} - \frac{1}{3}(\nabla \cdot \mathbf{u})\delta_{ij}\right) = \eta\left(\nabla \mathbf{u} + (\nabla \mathbf{u})^{\top}\right) - \frac{2}{3}\eta(\nabla \cdot \mathbf{u})I$$

where η is the dynamic viscosity, I the identity tensor and the second term on the right-hand side will vanish in an incompressible model. Buoyancy forces result from changes in local density, which are primarily driven by deviations in temperature T. The latter needs to satisfy a time-dependent advection-diffusion equation of the form

$$\frac{\partial T}{\partial t} = \nabla \cdot (k \nabla T) - (\mathbf{u} \cdot \nabla)\, T + f_T(x, T, p, \mathbf{u}) \ . \tag{2}$$

ICCS Camera Ready Version 2024
To cite this paper please use the final published version:
DOI: 10.1007/978-3-031-63759-9_33

The term f_T encompasses various possible heat sources, such as shear, adiabatic or radiogenic heating. The system then needs to be closed by selecting an appropriate equation of state to couple density to pressure and temperature. It is known that the hydrostatic density of the mantle increases by a factor of about two from the surface to the core-mantle boundary (CMB). Hence, a purely incompressible flow model will not be exact. A common approach in Geodynamics is to select a reference state $(\bar{p}, \bar{T})$, from which one derives $\bar{\rho}$, and express quantities of interest as deviations from this reference state, e.g. $T = \bar{T} + T'$. Commonly these reference states are only depth-dependent and time invariant. Buoyancy forces arise from deviations ρ' to the radial background model $\bar{\rho}$, but are assumed to be much smaller than the latter. They can, thus, be neglected in the continuity equation, which avoids pressure waves in the model, but must, of course, be considered in the momentum equation, through T'. In total one commonly employs the truncated anelastic liquid approximation, see e.g. [11, 16] and uses the following system of non-dimensional equations

$$-\nabla \cdot \tau + \nabla p' = -\mathrm{Ra}\bar{\rho}\alpha g T' \tag{3}$$

$$\nabla \cdot (\bar{\rho}\mathbf{u}) = 0 \tag{4}$$

$$\bar{\rho}c_p \frac{DT'}{Dt} + \mathrm{Di}\bar{\rho}\alpha w(T' + T_s) - \nabla \cdot (k\nabla T) = \frac{\mathrm{Di}}{\mathrm{Ra}}\Phi \tag{5}$$

where $w = -g \cdot \mathbf{u}$, Ra and Di are the Rayleigh and dissipation number respectively, $\Phi = \tau : \dot{\epsilon}$ describes shear heating and $\frac{D}{Dt}(\cdot)$ is the material derivative while c_p, k, α, and T_s are the non-dimensionalised coefficients of heat capacity, diffusivity, thermal expansivity and the surface temperature.

In a typical, so-called *mantle circulation model*, Earth's mantle is modeled by a thick spherical shell. Temperature is fixed on the top and bottom by imposing Dirichlet boundary conditions. The tangential components of the velocity are taken from paleo-reconstructions of the movement of tectonic plates, while one requires the radial component to vanish. So one has a *no outflow* condition. At the CMB one also requires no outflow and combines this with the constraint of vanishing shear-stress, as the rocky mantle slides freely on the molten iron of the outer core. Formally one requires

$$\begin{aligned} \mathbf{u} \cdot \mathbf{n} &= 0 && \text{on } \Gamma_{\mathrm{surf}} \cup \Gamma_{\mathrm{CMB}} \\ \mathbf{u} \cdot \mathbf{t} &= \mathbf{u}_{\mathrm{plate}} \cdot \mathbf{t} && \text{on } \Gamma_{\mathrm{surf}} \\ \mathbf{t} \cdot \tau \cdot \mathbf{n} &= 0 && \text{on } \Gamma_{\mathrm{CMB}} \end{aligned}$$

with $\mathbf{n}$ being the normal vector in a point and $\mathbf{t}$ any vector in the tangential plane. The combination of vanishing shear stress with no outflow constitutes a freeslip boundary condition.

3 Software Framework – HyTeG

In this contribution we consider the solution of mantle convection problems using the finite element framework HyTeG (Hybrid Tetrahedral Grids) [18, 21].

ICCS Camera Ready Version 2024
To cite this paper please use the final published version:
DOI: 10.1007/978-3-031-63759-9_33

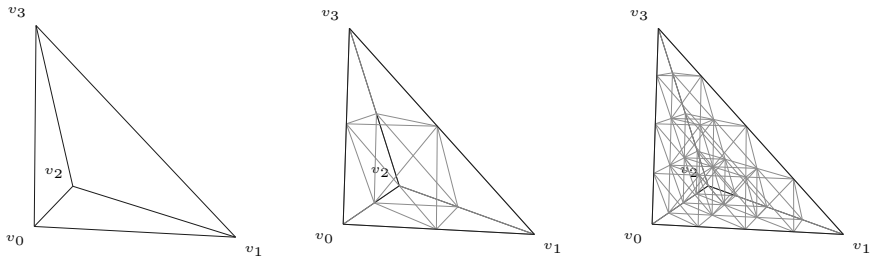

(a) *coarse grid tetrahedron* (b) *one refinement iteration* (c) *two refinement iterations*

Fig. 1: *Uniform refinement of a single coarse grid element.*

HyTeG enables the solution of partial differential equations at the extreme-scale through massively parallel matrix-free geometric multigrid methods. The mesh hierarchy is constructed based on an unstructured triangular or tetrahedral base mesh by successive steps of uniform refinement. Figure 1 illustrates the regular refinement of a single coarse grid element. This results in an L-level hierarchy $\mathcal{T}_\ell$, $\ell = 0, \ldots, L-1$, with $\mathcal{T}_0$ being the unstructured coarse mesh. The compute kernels, then, take advantage of the resulting block-structured domain partitioning, while the mesh hierarchy supports construction of geometric multigrid solvers. Details on the refinement and finite element data structures are presented in [18].

HyTeG's extreme scalability and performance was demonstrated in, e.g., [20], where Stokes systems with more than a trillion ($> 10^{12}$) unknowns were solved on up to 147,456 parallel processes. Such problem sizes are only feasible due to extremely memory-efficient solvers with optimal time complexity such as the employed matrix-free multigrid methods. For strongly advection-dominated flows, that are relevant in mantle convection models, HyTeG implements a massively parallel Eulerian-Lagrangian method that handles the advective terms through a particle-based implementation of the modified method of characteristics (MMOC) [19].

4 Finite Element Discretization

We discretise the Stokes equations, (3) and (4), of the convection model by means of $P_2 - P_1$ Taylor-Hood elements to approximate velocity $\mathbf{u}$ and pressure p. This gives us the discrete weak formulation of the problem as: find $(\mathbf{u}_h, p_h) \in \mathcal{U}_h \times \mathcal{P}_h$ such that

$$\int_\Omega \boldsymbol{\tau} : \nabla \mathbf{v}_h - \int_\Omega p_h \nabla \cdot \mathbf{v}_h = \int_\Omega -\mathrm{Ra}\bar{\rho}\alpha T' \mathbf{g} \cdot \mathbf{v}_h \tag{6}$$

$$-\int_\Omega q_h \nabla \cdot (\bar{\rho}\mathbf{u}_h) = 0 \tag{7}$$

holds for all $(\mathbf{v}_h, q_h) \in \mathcal{U}_h \times \mathcal{P}_h$, with

$$\mathcal{U}_h = \left(P_2 \cap H_0^1\right)^3 \quad , \quad \mathcal{P}_h = P_1 \cap H^0 \quad .$$

ICCS Camera Ready Version 2024
To cite this paper please use the final published version:
DOI: 10.1007/978-3-031-63759-9_33

Here H_0^1 contains all functions from the standard Sobolev space H^1, whose trace equals zero on the Dirichlet part Γ_D of the domain boundary. Uniqueness of pressure within $\mathcal{P}_h$ is enforced by requiring that the average over all degrees of freedom (DoFs) vanishes.

We handle compressibility in the continuity equation by the frozen velocity approach, see e.g. [14], i.e., we rewrite (7) as

$$\int_\Omega q_h \nabla \cdot \mathbf{u}_h(t+\delta t) = \int_\Omega -q_h \left(\frac{\nabla \bar{\rho}}{\bar{\rho}} \cdot \mathbf{u}_h(t) \right) \tag{8}$$

which means that the associated bilinear form, when solving for the velocity at the new timestep, is the same as in the incompressible case. The energy equation (5) can formally be re-written as

$$\frac{\partial T'}{\partial t} + \mathbf{u} \cdot \nabla T = \mathcal{F}(t, T', \mathbf{u}) \ , \tag{9}$$

where $\mathcal{F}$ includes diffusion. We approximate T with P_2 elements and apply a splitting approach, where the advective component is resolved with the MMOC [19]. Here virtual particles corresponding to the DoFs of $T_h(t+\delta t)$ are advected back in time along characteristics to obtain their departure points $\boldsymbol{x}_{\text{dept}}$ at time t. A Runge-Kutta scheme of order 4 is used to solve the resulting ordinary differential equations (ODEs). With this, the energy equation can then be semi-discretised in time as

$$\frac{T'(\boldsymbol{x}, t+\delta t) - \hat{T}'(\boldsymbol{x}, t)}{\delta t} \approx \Theta \mathcal{F}(\boldsymbol{x}, t+\delta t, T', \mathbf{u}_h) + (1-\Theta)\mathcal{F}(\boldsymbol{x}, t, \hat{T}', \mathbf{u}_h) \tag{10}$$

where $\hat{T}'(\boldsymbol{x}, t) = T'(\boldsymbol{x}_{\text{dept}}, t)$. For a full derivation and other variants available in HyTeG see [19].

With this we proceed in solving the coupled system (3) to (5) according to Algorithm 1. For each step at time t, the δt for the energy equation is computed with the Courant–Friedrichs–Lewy (CFL) condition based on the velocity field at time t. After obtaining the temperature field at time $(t+\delta t)$ by solving (9) and (10), the corresponding velocity field at $(t+\delta t)$ is obtained by solving (6) and (7). Under the assumption that a single Picard type iteration is enough to couple the Stokes and energy equation, we perform a single solve of each in every timestep. Note that the MMOC is not formally bound to the CFL. In [19] it was demonstrated that, with a more sophisticated splitting approach, δt's exceeding this condition are permissible.

The geometry of the Earth's mantle is approximated in our models in 2D by an annulus and in 3D by a thick spherical shell. The corresponding meshes are illustrated in Figures 2b and 2c. We apply projections from the computational polyhedral meshes to the non-polyhedral physical domains to exactly capture the curvature of the boundaries. These so called blending maps are incorporated into the finite element integrals, see [2] for details.

ICCS Camera Ready Version 2024
To cite this paper please use the final published version:
DOI: 10.1007/978-3-031-63759-9_33

Algorithm 1: Coupled timestepping algorithm

```
initialise T';
solve Stokes system (6) and (7) for u_h;
t ← t_0;
while t < t_end do
    calculate timestep size δt using u_h(t) for the CFL condition;
    execute advection step by calculating x_dept and evaluating T̂';
    solve (10) for T' (with Θ = 1.0);
    solve (6) and (7) for u_h (using new T');
    t ← t + δt;
end
```

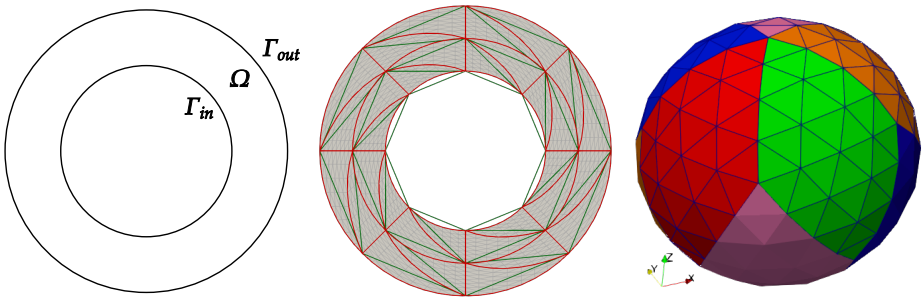

(a) (b) (c)

Fig. 2: *Visualizations of domain and mesh. Figure 2a: schematic sketch of the annulus domain with inner and outer boundaries* Γ_{in} *and* Γ_{out}*. Figure 2b: computational coarse mesh* $\mathcal{T}_0$ *without projection (green) overlayed by the projected mesh after refinement to* $\mathcal{T}_3$ *(macro-element boundaries in red, micro-elements in grey). Figure 2c: computational coarse mesh* $\mathcal{T}_0$ *of the spherical shell (without projection).*

5 Results and Discussion

In this section, we present results for a number of standard benchmarks used in the Geodynamics community, before demonstrating applicability of our code to model convection in an Earth-like setting.

5.1 Stationary Benchmarks – Stokes System

Here we assess the convergence of the computed finite element approximation to analytical solutions of the Stokes system (1) and (4). To approximate the mantle, we define Ω (annulus in 2D, thick spherical shell in 3D) with inner radius $r_{\text{min}} = 1.22$ and outer radius $r_{\text{max}} = 2.22$, thereby maintaining a ratio of $\frac{1.22}{2.22} \simeq 0.55$, which is close to the actual ratio for Earth, while also maintaining the non-dimensional thickness of the mantle to be $\Delta r = r_{\text{max}} - r_{\text{min}} = 1.0$. The forcing function, driving the flow, models a density anomaly, which from (1)

ICCS Camera Ready Version 2024
To cite this paper please use the final published version:
DOI: 10.1007/978-3-031-63759-9_33

becomes $-g\rho'\hat{\mathbf{r}}$, with $\bar{\rho} = 0$ and $\hat{\mathbf{r}}$ is a unit vector pointing outward (opposite to gravity). For the annulus, the forcing is based on a cosine term, while for the spherical shell it is based on the spherical harmonics function $Y_{\ell m}$ of degree ℓ and order m.

We follow [22] and perform experiments for two choices of ρ':

Smooth forcing

$$\rho' = \left(\frac{r}{r_{\max}}\right)^k \cos(n\phi) \text{ in 2D }, \quad \rho' = \left(\frac{r}{r_{\max}}\right)^k Y_{\ell m}(\theta, \phi) \text{ in 3D}, \tag{11}$$

δ-function forcing

$$\rho' = \delta(r - r')\cos(n\phi) \text{ in 2D}, \quad \rho' = \delta(r - r')Y_{\ell m}(\theta, \phi) \text{ in 3D}, \tag{12}$$

where k, n are constants while ϕ refers to the angle with the x-axis in 2D and θ, ϕ refer to the co-latitude and longitude respectively in 3D. In the δ-function forcing case, the 3D volume integral in the finite element discrete form over the right-hand side of (1) reduces to a surface integral

$$\int_\Omega -g\rho'\hat{\mathbf{r}} \cdot \mathbf{v}_h d\Omega = \int_\Omega -g\delta(r - r')Y_{\ell m}\hat{\mathbf{r}} \cdot \mathbf{v}_h d\Omega = \int_{\Gamma'} -gY_{\ell m}\hat{\mathbf{r}} \cdot \mathbf{v}_h d\Gamma',$$

where Γ' is the spherical surface of radius r'. We design our mesh in such a way that Γ' is discretised by tetrahedral faces. The analogous reduction and meshing applies to the 2D case.

Two sets of boundary conditions are considered, a freeslip boundary condition on the inner boundary and a noslip condition on the outer boundary, denoted by noslip-freeslip ($\Gamma_{in} = \Gamma_{FS}, \Gamma_{out} = \Gamma_D$, see Figure 2a), and another type where only freeslip is considered on both the boundaries, denoted by freeslip-freeslip ($\Gamma_{in} = \Gamma_{FS}, \Gamma_{out} = \Gamma_{FS}$, see Figure 2a). The analytical solutions for the freeslip-freeslip case are available through the Python package *assess* from [22], where the general form of the solution has been derived for the annulus and spherical shell. Hence, we use the same form and derive the respective coefficients for noslip-freeslip boundary condition setup by means of computer algebra.

In the 2D annulus mesh, as shown in Figure 2b, at $\mathcal{T}_0$, we consider 8 layers in tangential direction and 2 layers in radial direction at the coarsest level. For the 3D shell mesh, we use the icosahedral meshing approach [8], which results in ten diamond shaped sections. Figure 2c shows a top view of the North pole, where five sections meet. The resolution of the base mesh is defined by two parameters. One is the number of divisions along the curved edges of each section, the other the number of layers in radial direction. We use as starting mesh for our convergence study $\mathcal{T}_2$, which contains $\simeq 10^2$ triangles with $\simeq 3 \times 10^4$ DoFs for the annulus and $\simeq 10^5$ tetrahedrons with $\simeq 3 \times 10^7$ DoFs for the spherical shell.

For this study, we use the Minres solver for the Stokes system with a lumped inverse mass matrix preconditioner [10] for the Schur complement. At the freeslip boundary, the velocity field is projected such that the normal component is zero at every step of the iterative solver.

ICCS Camera Ready Version 2024
To cite this paper please use the final published version:
DOI: 10.1007/978-3-031-63759-9_33

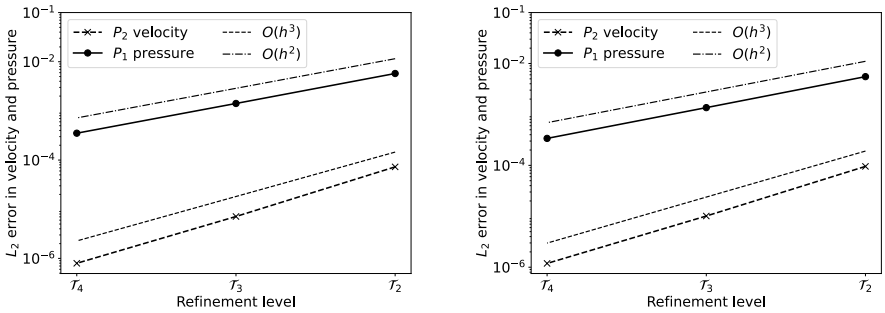

(a) *noslip-freeslip, smooth forcing, 2D* (b) *freeslip-freeslip, smooth forcing, 2D*

Fig. 3: *L_2-errors of velocity and pressure, smooth forcing on the annulus with $n = 2, k = 2$ in* (11).

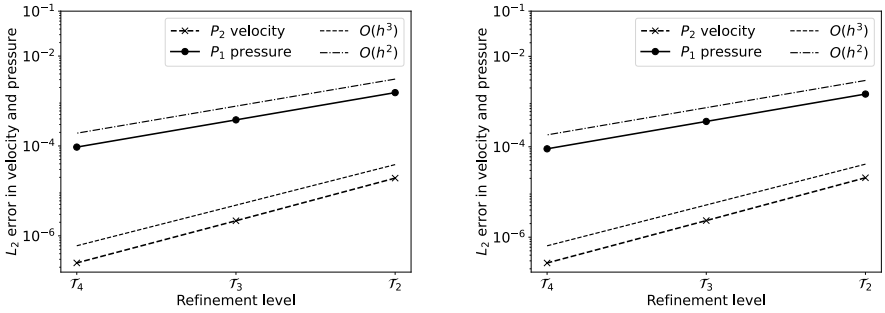

(a) *noslip-freeslip, smooth forcing, 3D* (b) *freeslip-freeslip, smooth forcing, 3D*

Fig. 4: *L_2-errors of velocity and pressure, smooth forcing on the spherical shell with $\ell = 2, m = 2, k = 2$ in* (11).

Let $\mathbf{u}_h$ be the discrete solution on level ℓ. Then we approximate the velocity error $\mathbf{e} = \mathbf{u} - \mathbf{u}_h$ and its L_2-norm by interpolating both $\mathbf{u}$ and $\mathbf{u}_h$ in the FE space for $\mathcal{T}_{\ell+1}$ and evaluating it there, similar for pressure. With smooth forcing, for both noslip-freeslip and freeslip-freeslip, we obtain the theoretically expected L_2 convergence rates under refinement [12], i.e. cubic, $\mathcal{O}(h^3)$, for velocity and quadratic, $\mathcal{O}(h^2)$, for pressure, for both the annulus and spherical shell as can be seen in Figures 3 and 4. For the δ-function forcing cases, the convergence speed deteriorates. We observe only $\mathcal{O}(h^{1.5})$ for velocity and $\mathcal{O}(h^{0.5})$ for pressure. See Figures 5 and 6. This behaviour is consistent with [22]. The analytical pressure solution for the δ-function forcing is a discontinuous function. As the P_1 finite element can only represent continuous functions, we should expect to see an impact on its convergence and in turn for the velocity as well. The convergence properties can be regained by choosing a discontinuous pressure element. A more

ICCS Camera Ready Version 2024
To cite this paper please use the final published version:
DOI: 10.1007/978-3-031-63759-9_33

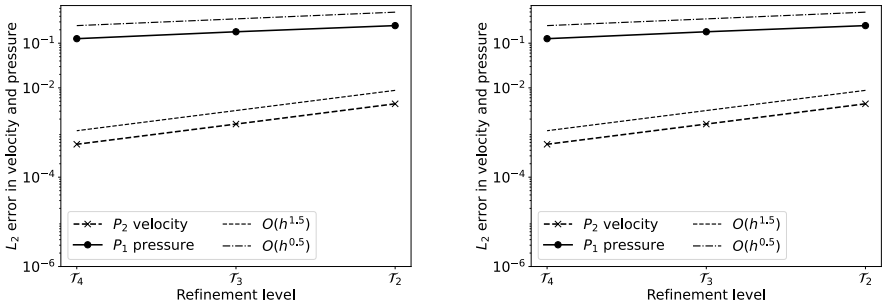

(a) *noslip-freeslip, delta forcing, 2D* (b) *freeslip-freeslip, delta forcing, 2D*

Fig. 5: *L_2-errors of velocity and pressure, delta forcing on annulus with $n = 2$ in* (12).

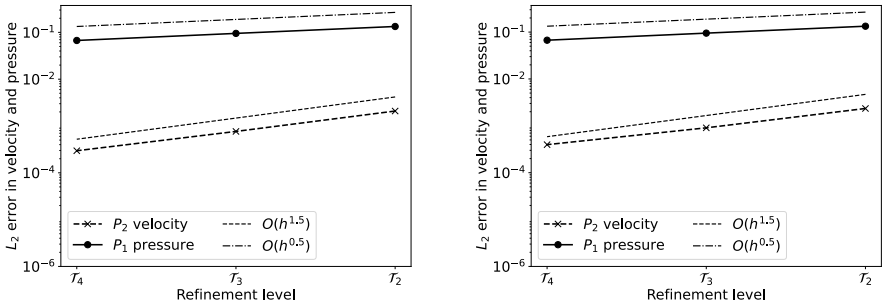

(a) *noslip-freeslip, delta forcing, 3D* (b) *freeslip-freeslip, delta forcing, 3D*

Fig. 6: *L_2-errors of velocity and pressure, delta forcing on spherical shell with $\ell = 2, m = 2$ in* (12).

detailed discussion and an example with an enriched P_2-element for velocity and a discontiunous P_1 element for pressure can be found in [22].

5.2 Time Dependent Benchmarks – Unit Square

In this section, we present a benchmark from [3], specifically case 1a, where a suite of software codes for modelling convection processes were compared. The problem considers an isoviscous, bottom heated model on a unit square. The idea is to prescribe a sinusoidal perturbation of temperature given by

$$T(x, y, t = 0) = (1 - y) + A\cos(\pi x)\sin(\pi y), \text{ with } A = 0.05 \ , \qquad (13)$$

while imposing freeslip boundary conditions for the velocity on all four walls of the box. For the temperature field, a Dirichlet boundary condition of $T = 0$ and $T = 1$ is imposed at the top and bottom respectively, while zero flux is imposed

ICCS Camera Ready Version 2024
To cite this paper please use the final published version:
DOI: 10.1007/978-3-031-63759-9_33

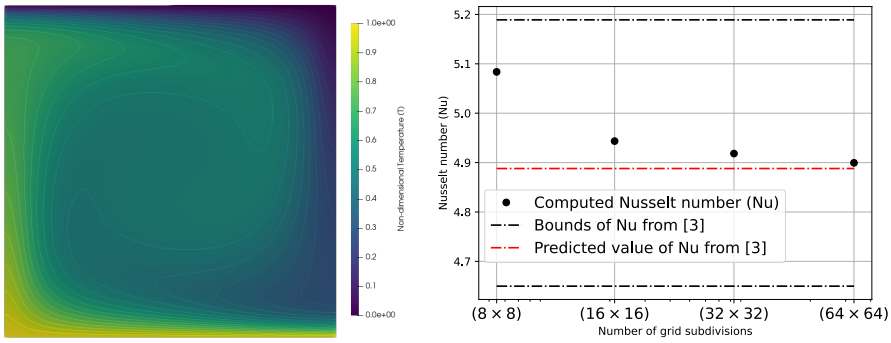

(a) *Non-dimensional temperature field with isolines*

(b) *Nu vs Number of DoFs*

Fig. 7: *Convection on a square after reaching steady state.*

at the vertical sides. The perturbation combined with the freeslip boundary condition induces a single convection cell in the square and heat advects and diffuses to reach a steady state. Once this state is reached, the Nusselt number is calculated at the top boundary. The latter gives an estimate of the amount of heat transported by advection and diffusion to that of pure diffusion.

Equations (3) to (5) are solved according to Algorithm 1, but we consider the total temperature T instead of T' with no internal heating, $\mathrm{Di} = 0$, $c_p = 1$ and an isoviscous, incompressible model with constant density $\bar{\rho} = 1$, $\eta = 1$ and $\mathbf{g} = [0, -1]^\top$. The experiments are performed with $\mathrm{Ra} = 10^4$ and the Nusselt number (Nu) for the top boundary of the unit square is calculated via

$$\mathrm{Nu} = \frac{\int_0^1 \frac{\partial T(x,1)}{\partial y} dx}{\int_0^1 T(x,0) dx} \ , \tag{14}$$

as in [3]. To verify our implementation, we choose our mesh based on the range of resolutions in [3] and compare the computed Nusselt numbers to the values obtained by other codes. With refinement, our computed results converge to the values reported in the benchmark and stay in the range of values predicted by other codes, see Figure 7.

5.3 Time Dependent Benchmarks – Thick Spherical Shell

In addition to the previous 2D benchmarks, we now perform computations on a thick spherical shell and verify our implementation through the community benchmark described in [6, 26]. It involves simulation of convection behaviour on a thick spherical shell by imposing freeslip boundary conditions for the velocity

ICCS Camera Ready Version 2024
To cite this paper please use the final published version:
DOI: 10.1007/978-3-031-63759-9_33

field on both Γ_{in} and Γ_{out}, while a Dirichlet boundary condition is specified for the temperature field with $T = 0$ on Γ_{out} and $T = 1$ on Γ_{in}. The initial condition for the temperature is given by

$$T(\boldsymbol{x}, 0) = T_c(\boldsymbol{x}) + AY_{\ell m}(\theta, \phi)\sin(\pi(r - r_{\min})),$$

with $A = 0.04$, $(\ell, m) = (3, 2)$ and the background profile,

$$T_c(\boldsymbol{x}) = \left(\frac{r_{\min} r_{\max}}{r}\right) - r_{\min}.$$

The temperature deviations from the background profile due to this specific spherical harmonic induces four plumes to rise up and stabilize with time in a tetrahedral symmetry around the center. When the Rayleigh number increases, the convective vigour increases and the plumes get thinner. This can be seen from larger velocity magnitudes and higher Nusselt numbers, which vary proportional to the third root of the Rayleigh number [9], $\text{Nu} \simeq \text{Ra}^{\frac{1}{3}}$. For a spherical surface Γ at radius r, the Nusselt number is calculated by

$$\text{Nu} = \frac{\int_\Gamma \frac{\partial T}{\partial r} d\Gamma}{\int_\Gamma \frac{\partial T_c}{\partial r} d\Gamma}. \tag{15}$$

Ideally the Nusselt number must be the same for $r \in [r_{\min}, r_{\max}]$. We choose $r = r_{\min}$ for the evaluation.

Equations (3) to (5) are solved according to Algorithm 1, but we consider the total temperature T instead of T' with $\text{Di} = 0$, $c_p = 1$, constant density $\bar{\rho} = 1$ with $\mathbf{g} = -\hat{\mathbf{r}}$ and different Rayleigh numbers. The experiments are performed on an icosahedral mesh with roughly 10^6 temperature DoFs. Figure 8 shows the iso-surface of the non-dimensional temperature at $T = 0.5$ and how the plume shape changes with the Rayleigh number. Figure 9a shows the Rayleigh number dependent variation of the Nusselt number, which obeys the cubic proportionality as expected. An inference to note is that [26] concludes with a proportionality of $\text{Nu} \simeq \left({}^{\text{Ra}}/_{\text{Ra}_{\text{crit}}}\right)^{1/4}$, where Ra_{crit} is the Rayleigh number at the onset of convection, which is constant for a given temperature dependent viscosity law. But for the Rayleigh number range and the isoviscous case that we have considered, a cubic proportionality between Nu and Ra is seen which also corroborates with the values from [26], as seen in Figure 9a.

5.4 Mantle Convection

Here we show results from a model based on the Truncated Anelastic Liquid Approximation (TALA) formulation which is currently under development. This is being done with the software framework HyTeG under the TerraNeo project, the goal of which is to create a scalable and accurate Earth model which can be used for various geophysical applications.

ICCS Camera Ready Version 2024
To cite this paper please use the final published version:
DOI: 10.1007/978-3-031-63759-9_33

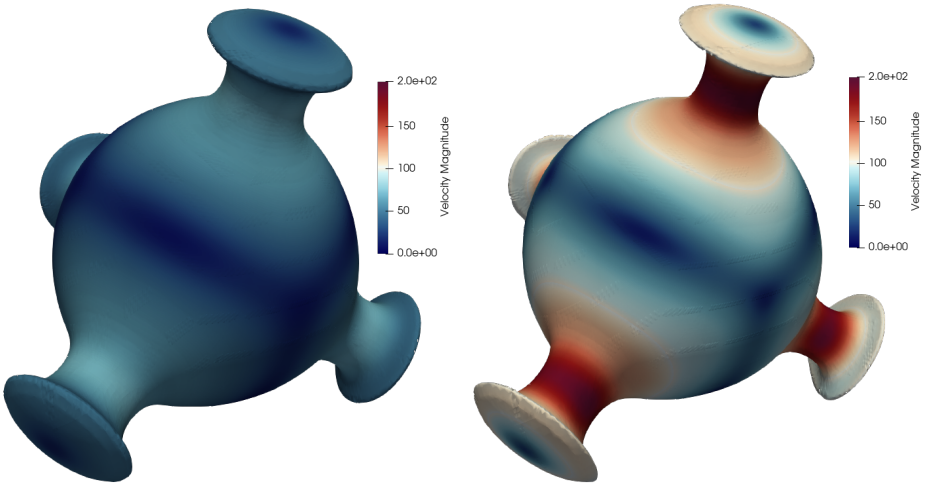

(a) *Rayleigh number* $= 7 \times 10^3$ (b) *Rayleigh number* $= 2 \times 10^4$

Fig. 8: *Iso-surface of non-dimensional temperature at* $T = 0.5$ *coloured by magnitude of velocity for comparison between Rayleigh numbers after reaching steady state*

Equations (3) to (5) are solved according to Algorithm 1. An implicit Euler scheme with $\Theta = 1.0$ in (10) is used for the time discretization of the diffusive and other forcing terms in (5). The Stokes system is solved with a monolithic geometric multigrid method that uses an inexact Uzawa method for relaxation, see [20] for details. The base mesh $\mathcal{T}_0$ is a thick spherical shell represented by an icosahedral mesh composed of $\simeq 10^3$ tetrahedrons. This is taken as the coarsest level for the V-cycle of the multigrid algorithm and $\mathcal{T}_4$ for the finest level, which then contains $\simeq 3 \times 10^7$ DoFs for the Stokes system and $\simeq 1 \times 10^7$ DoFs for temperature. The model is isoviscous with $\eta = 1$, compressible with the radially varying density profile given by

$$\bar{\rho} = \bar{\rho}_s \exp\left(\frac{\mathrm{Di}(r_{\max} - r)}{\mathrm{Gr}(r_{\max} - r_{\min})}\right) \quad , \tag{16}$$

where $\bar{\rho}_s = 1$ here and Gr is the Grüneisen parameter [17]. The values considered are $\mathrm{Ra} = 10^5$ and $T_s = 0$ while all other nondimensional parameters are set to 1 and no-slip boundary conditions are considered both on the surface ($r_{\max}$) and CMB ($r_{\min}$). Around the CMB, we prescribe the initial temperature deviation

$$T'(\boldsymbol{x}, 0) = T'_0 \exp\left(-A\frac{r - r_{\min}}{r_{\max} - r_{\min}}\right) Y_{\ell m}(\theta, \phi) \tag{17}$$

with scaling factors T'_0 and A, and a spherical harmonics function of order $\ell = 6$ and degree $m = 4$, which then induces plumes according to the harmonic that rise up to the surface, see Figure 9b.

ICCS Camera Ready Version 2024
To cite this paper please use the final published version:
DOI: 10.1007/978-3-031-63759-9_33

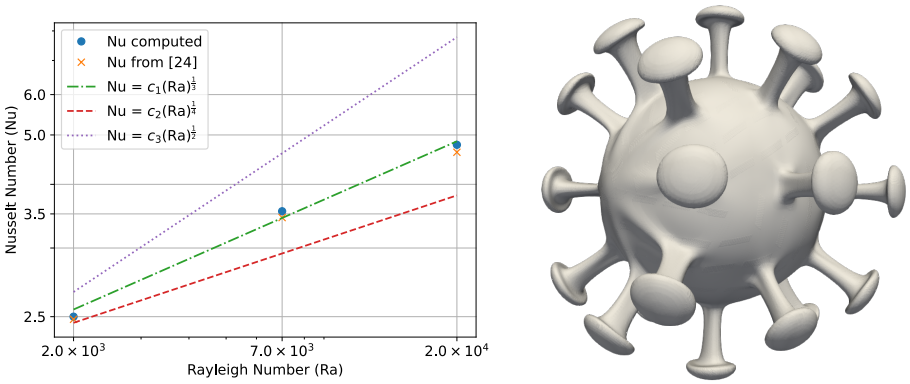

(a) *Nu vs Ra from section 5.3*

(b) *Compressible mantle convection, Ra* $= 10^5$

Fig. 9: *Variation of Nusselt number with respect to Rayleigh number for the tetrahedral symmetry case from section 5.3 (left), Compressible Mantle convection model with adiabatic density profile showing non-dimensional temperature iso-surfaces (right)*

The results are obtained from running the model on our in-house cluster TETHYS-3g [24] which is composed of 24 AMD EPYC 7662 processors for a total of 1536 cores connected via 100 GBit/s Infiniband HDR. For the export of 3D data, the ADIOS2 package [13], which is developed for IO operations especially on supercomputers, is employed in our framework.

6 Conclusion

In this paper, we have verified the implementation of a model for mantle convection simulation in the HyTeG finite element framework against different semi-analytical setups and community benchmarks. The agreement of our numerical results with the literature demonstrates its applicability for Geophysical applications. First, we showed the numerical convergence of our approximation to the solution of a Stokes system for cases with different boundary conditions and different forcing terms. Then we showcased the capability of our framework to solve transport equations and verified it through time-dependent benchmark problems. Finally, we showed results for a model based on the TALA formulation. Future work will include benchmarking against temperature dependent viscosity cases and nonlinear rheologies.

Acknowledgements

Funding was provided by the German Research Foundation (DFG) research training group UPLIFT 440512084 (GRK 2698) and the German Ministry of

ICCS Camera Ready Version 2024
To cite this paper please use the final published version:
DOI: 10.1007/978-3-031-63759-9_33

Research and Education (BMBF) via its SCALEXA initiative (project CoMPS). Computing resources were provided by the Institute of Geophysics of LMU Munich [24] funded by DFG 495931446.

References

1. Bauer, S., Bunge, H.P., Drzisga, D., Ghelichkhan, S., Huber, M., Kohl, N., Mohr, M., Rüde, U., Thönnes, D., Wohlmuth, B.: TerraNeo — Mantle Convection Beyond a Trillion Degrees of Freedom. In: Bungartz, H.J., Reiz, S., Uekermann, B., Neumann, P., Nagel, W. (eds.) Software for Exascale Computing - SPPEXA 2016-2019. Lecture Notes in Computational Science and Engineering, vol. 136, pp. 569–610. Springer (2020). https://doi.org/10.1007/978-3-030-47956-5_19
2. Bauer, S., Mohr, M., Rüde, U., Weismüller, J., Wittmann, M., Wohlmuth, B.: A two-scale approach for efficient on-the-fly operator assembly in massively parallel high performance multigrid codes. Appl. Numer. Math. **122**, 14–38 (2017). https://doi.org/10.1016/j.apnum.2017.07.006
3. Blankenbach, B., Busse, F., Christensen, U., Cserepes, L., Gunkel, D., Hansen, U., Harder, H., Jarvis, G., Koch, M., Marquart, G., Moore, D., Olson, P., Schmeling, H., Schnaubelt, T.: A benchmark comparison for mantle convection codes. Geophys. J. Int. **98**(1), 23–38 (1989). https://doi.org/10.1111/j.1365-246X.1989.tb05511.x
4. Brown, H., Colli, L., Bunge, H.P.: Asthenospheric flow through the Izanagi-Pacific slab window and its influence on dynamic topography and intraplate volcanism in East Asia. Frontiers in Earth Science **10** (2022). https://doi.org/10.3389/feart.2022.889907
5. Bunge, H.P., Richards, M., Baumgardner, J.: A sensitivity study of three-dimensional spherical mantle convection at 10^8 Rayleigh number: Effects of depth-dependent viscosity, heating mode, and an endothermic phase change. JGR: Solid Earth **102**(B6), 11991–12007 (1997). https://doi.org/10.1029/96JB03806
6. Burstedde, C., Stadler, G., Alisic, L., Wilcox, L.C., Tan, E., Gurnis, M., Ghattas, O.: Large-scale adaptive mantle convection simulation. Geophys. J. Int. **192**(3), 889–906 (2013). https://doi.org/10.1093/gji/ggs070
7. Christensen, U., Yuen, D.: Layered convection induced by phase transitions. JGR: Solid Earth **90**(B12), 10291–10300 (1985). https://doi.org/10.1029/JB090iB12p10291
8. Davies, D.R., Davies, J.H., Bollada, P.C., Hassan, O., Morgan, K., Nithiarasu, P.: A hierarchical mesh refinement technique for global 3-D spherical mantle convection modelling. Geosci. Model Dev. **6**(4), 1095–1107 (2013). https://doi.org/10.5194/gmd-6-1095-2013
9. Davies, G.: Dynamic Earth: Plates, Plumes and Mantle Convection. Cambridge University Press (1999)
10. Elman, H., Silvester, D., Wathen, A.: Finite Elements and Fast Iterative Solvers: with Applications in Incompressible Fluid Dynamics. Oxford University Press (06 2014)
11. Gassmöller, R., Dannberg, J., Bangerth, W., Heister, T., Myhill, R.: On formulations of compressible mantle convection. Geophys. J. Int. **221**(2), 1264–1280 (2020). https://doi.org/10.1093/gji/ggaa078
12. Girault, V., Raviart, P.A.: Incompressible Mixed Finite Element Methods for Solving the Stokes Problem. In: Girault, V., Raviart, P.A. (eds.) Finite Element Methods for Navier-Stokes Equations: Theory and Algorithms, pp. 193–277. Springer (1986). https://doi.org/10.1007/978-3-642-61623-5_3

ICCS Camera Ready Version 2024
To cite this paper please use the final published version:
DOI: 10.1007/978-3-031-63759-9_33

13. Godoy, W.F., Podhorszki, N., et al.: ADIOS 2: The Adaptable Input Output System. A framework for high-performance data management. SoftwareX **12** (Jul 2020). https://doi.org/10.1016/j.softx.2020.100561
14. Heister, T., Dannberg, J., Gassmöller, R., Bangerth, W.: High accuracy mantle convection simulation through modern numerical methods – II: realistic models and problems. Geophys. J. Int. **210**(2), 833–851 (2017). https://doi.org/10.1093/gji/ggx195
15. Horbach, A., Bunge, H.P., Oeser, J.: The adjoint method in geodynamics: derivation from a general operator formulation and application to the initial condition problem in a high resolution mantle circulation model. Int. J. Geomath. **5**(2), 163–194 (2014). https://doi.org/10.1007/s13137-014-0061-5
16. Jarvis, G., Mckenzie, D.: Convection in a compressible fluid with infinite Prandtl number. J. Fluid. Mech. **96**(3), 515–583 (1980). https://doi.org/10.1017/S002211208000225X
17. King, S.D., Lee, C., Van Keken, P.E., Leng, W., Zhong, S., Tan, E., Tosi, N., Kameyama, M.C.: A community benchmark for 2-D Cartesian compressible convection in the Earth's mantle. Geophys. J. Int. **180**(1), 73–87 (2010). https://doi.org/10.1111/j.1365-246X.2009.04413.x
18. Kohl, N., Bauer, D., Böhm, F., Rüde, U.: Fundamental data structures for matrix-free finite elements on hybrid tetrahedral grids. Int. J. Parallel Emergent Distrib. Syst. **39**(1), 51–74 (2024). https://doi.org/10.1080/17445760.2023.2266875
19. Kohl, N., Mohr, M., Eibl, S., Rüde, U.: A Massively Parallel Eulerian-Lagrangian Method for Advection-Dominated Transport in Viscous Fluids. SIAM J. Sci. Comput. **44**(3), C260–C285 (2022). https://doi.org/10.1137/21M1402510
20. Kohl, N., Rüde, U.: Textbook Efficiency: Massively Parallel Matrix-Free Multigrid for the Stokes System. SIAM J. Sci. Comput. **44**(2), C124–C155 (2022). https://doi.org/10.1137/20M1376005
21. Kohl, N., Thönnes, D., Drzisga, D., Bartuschat, D., Rüde, U.: The *HyTeG* finite-element software framework for scalable multigrid solvers. Int. J. Parallel Emergent Distrib. Syst. **34**(5), 477–496 (Sep 2019). https://doi.org/10.1080/17445760.2018.1506453
22. Kramer, S.C., Davies, D.R., Wilson, C.R.: Analytical solutions for mantle flow in cylindrical and spherical shells. Geosci. Model Dev. **14**(4), 1899–1919 (2021). https://doi.org/10.5194/gmd-14-1899-2021
23. Oberbeck, A.: Über die Wärmeleitung der Flüssigkeiten bei Berücksichtigung der Strömungen infolge von Temperaturdifferenzen. Annalen der Physik **243**(6), 271–292 (1879). https://doi.org/10.1002/andp.18792430606
24. Oeser, J., Bunge, H.P., Mohr, M.: Cluster Design in the Earth Sciences: TETHYS. In: Gerndt, M., Kranzlmüller, D. (eds.) High Performance Computing and Communications – Second International Conference, HPCC 2006, Munich, Germany. Lecture Notes in Computer Science, vol. 4208, p. 31–40. Springer (2006). https://doi.org/10.1007/11847366_4
25. Oxburgh, E.R., Turcotte, D.L.: Mechanisms of continental drift. Rep Prog Phys **41**(8), 1249 (1978). https://doi.org/10.1088/0034-4885/41/8/003
26. Ratcliff, J.T., Schubert, G., Zebib, A.: Steady tetrahedral and cubic patterns of spherical shell convection with temperature-dependent viscosity. JGR: Solid Earth **101**(B11), 25473–25484 (1996). https://doi.org/https://doi.org/10.1029/96JB02097
27. Ricard, Y.: Physics of Mantle Convection. In: Bercovici, D. (ed.) Mantle Dynamics, Treatise on Geophysics, vol. 7, pp. 23–71. Elsevier, 2nd edn. (2015). https://doi.org/10.1016/B978-0-444-53802-4.00127-5

ICCS Camera Ready Version 2024
To cite this paper please use the final published version:
DOI: 10.1007/978-3-031-63759-9_33